

1 Contents

2	1	Experimental setup: Collider, detector and algorithms	1
3	1.1.	The Large Hadron Collider	3
4	1.2.	The CMS detector	5
5	1.2.1	The tracking system	6
6	1.2.2	The electromagnetic calorimeter	8
7	1.2.3	The hadronic calorimeter	9
8	1.2.4	The muon system	11
9	1.2.5	The trigger system	12
10	1.3.	Event reconstruction and particle identification	12
11	1.3.1	The particle-flow algorithm	13
12	1.3.2	Object reconstruction	14
13	1.3.2.1	Reconstruction of muons	16
14	1.3.2.2	Reconstruction of electrons	16
15	1.4.	Event simulation	17
16	2	Summary	19

17

Part 1

18

Experimental setup: Collider, detector and algorithms

19

²⁰ 1.1 The Large Hadron Collider

²¹ The Large Hadron Collider (LHC) [1, 2] is a particle accelerator installed in the former
²² LEP [3] tunnel at CERN [4]. It is 26.7 km in circumference and consists of two separate
²³ rings, which are, in periods of operation, inhabited by two counter-circulating beams.
²⁴ At the interaction points of the two beams, either proton-proton collisions or heavy ion
²⁵ collisions take place. In this thesis, only pp -collision data from the year 2012 is analysed.
²⁶ Thus, all machine values cited in the following chapters and paragraphs refer to the setup
²⁷ for pp -collisions in 2012 if not stated otherwise.

²⁸ The beams are separated into bunches which rotate with a bunch spacing of 50 ns
²⁹ corresponding to a collision frequency of 20 MHz. Before the bunches are actually filled
³⁰ into the LHC ring they are pre-accelerated in other accelerators, which are in the order
³¹ they are actually passed by the protons: Linac2, Proton Synchrotron Booster (PSB),
³² Proton Synchrotron (PS), Super Proton Synchrotron (SPS). The injector chain and the
³³ LHC ring with its experiments is visualised in Fig 1.1.

³⁴ In the LHC, the beams are kept on their circular path with the help of a magnetic field of

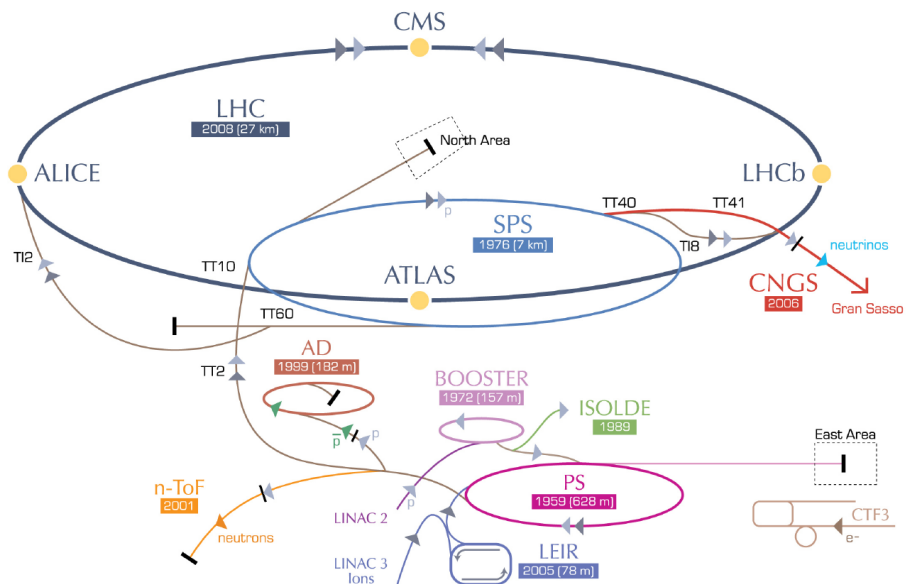


Figure 1.1: Visualisation of the LHC with its experiments and the injector chain. Taken from [5].

4.76 T. Further quadrupole and sextupole magnets squeeze and focus the bunches resulting in a bunch spread of roughly 8 cm length and a Gaussian shape radius of $20 \mu\text{m}$ RMS at the interaction point. The number of protons contained in each bunch is of the order 10^{11} . The LHC hosts four main particle physics experiments: the CMS, ATLAS, LHCb and ALICE experiments. CMS [6, 7] and ATLAS [8–10] are so-called “general purpose experiments”, that are used for a variety of different physics analyses. In contrast, the LHCb [11] and ALICE [12] experiments are designed with an emphasis on CP-violation measurements and heavy ion collisions, respectively. Each experiment is thus interested in different processes that happen at the beam collision points.

The number of expected events for a given process can be expressed in terms of the corresponding cross section σ times the integrated luminosity

$$N = L \cdot \sigma, \quad (1.1)$$

with an integrated luminosity of $L = \int \mathcal{L} dt$, where \mathcal{L} is the instantaneous luminosity. The instantaneous luminosity \mathcal{L} depends on several machine parameters, such as the collision frequency f , the number of particles in the bunches n_1 and n_2 , the spread in the transverse plane of the bunches σ_x and σ_y , and a geometrical correction parameter F due to the crossing angle of the two bunches at the interaction point:

$$\mathcal{L} = \frac{fn_1n_2}{4\pi\sigma_x\sigma_y} \cdot F. \quad (1.2)$$

In 2012, the peak luminosity was $7.7 \cdot 10^{33} \frac{1}{\text{cm}^2 \text{s}}$. The total integrated luminosity of pp -collisions over time recorded at the CMS experiment is shown in Fig. 1.2.

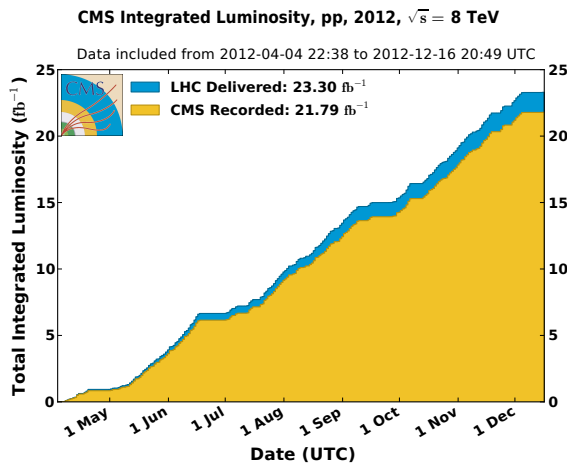


Figure 1.2: Integrated luminosity delivered by LHC (blue) and recorded by CMS (orange) in the year 2012. Taken from [13].

⁵³ 1.2 The CMS detector

⁵⁴ The Compact Muon Solenoid (CMS) detector [6, 7] is a general purpose detector, designed
⁵⁵ to explore particle physics phenomena up to the multi-TeV scale. The detector concept is
⁵⁶ an onion-like structure of different layers, each one made up of a different type of detector.
⁵⁷ The CMS detector measures 21.6 m in length and 14.6 m in diameter with a total weight
⁵⁸ of 12 500 tons. In Fig. 1.3, a perspective view of the CMS detector is depicted.

⁵⁹ The coordinate system used at CMS consists of the pseudorapidity $\eta = -\ln \tan \frac{\theta}{2}$ and
⁶⁰ the azimuthal angle ϕ . The advantage of the pseudorapidity η is the Lorentz invariance
⁶¹ with respect to the z-axis (beam axis). The angle ϕ covers the direction in the $x - y$ plane
⁶² (orthogonal to the beam axis).

⁶³ In order to measure the momentum of charged particles a superconducting solenoid is
⁶⁴ incorporated between the calorimeter system and the muon system providing a uniform
⁶⁵ axial magnet field of 3.8 T. Iron yokes contained within the muon system ensure the return
⁶⁶ of the magnetic flux.

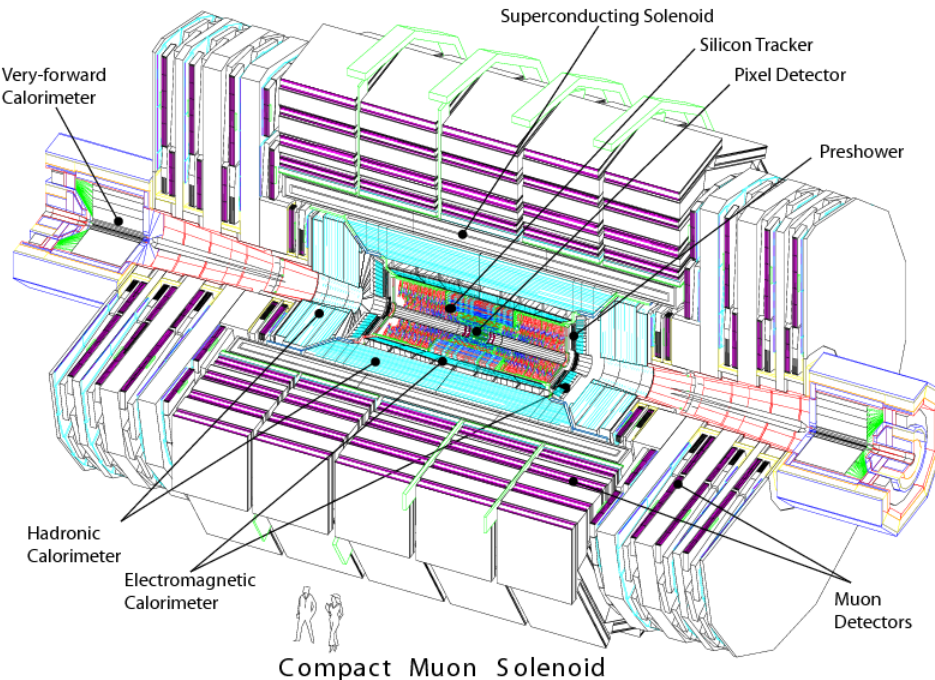


Figure 1.3: A perspective view of the CMS detector. Taken from [6]

67 In the following, the various detector components of the CMS detector from the inside
 68 to the outside as well as the trigger system will be explained.

69 1.2.1 The tracking system

70 The tracking detector [14–16] is the innermost detector at CMS. It is a silicon semicon-
 71 ductor detector and is included for the tasks of vertex and track reconstruction by the
 72 measurement of particles’ energy losses. A schematic sketch of the tracker at CMS is de-
 73 picted in Fig. 1.4. The tracking system is divided into two parts: the innermost tracker is
 74 a silicon pixel detector surrounded by a silicon strip detector. Both parts will be explained
 75 in detail in the upcoming sections, followed by a short description of how the energy of
 76 a traversing particle is measured with the silicon sensors. As a calibration of the silicon
 77 pixel detector was performed within this PhD thesis (see Section ??), an emphasis will be
 78 put on the pixel detector.

79 The silicon pixel tracker

80 The silicon pixel detector consists of three different cylindrical layers in the barrel region at
 81 radii of 4.4 cm, 7.3 cm and 10.2 cm and two discs in the endcaps at z -distances of 34.5 cm
 82 and 46.5 cm. It is made up of 1440 modules in total (barrel + endcaps), each module
 83 comprising 8 or 16 read-out-chips (ROCs). The read-out-chips are bump bonded [18] to a

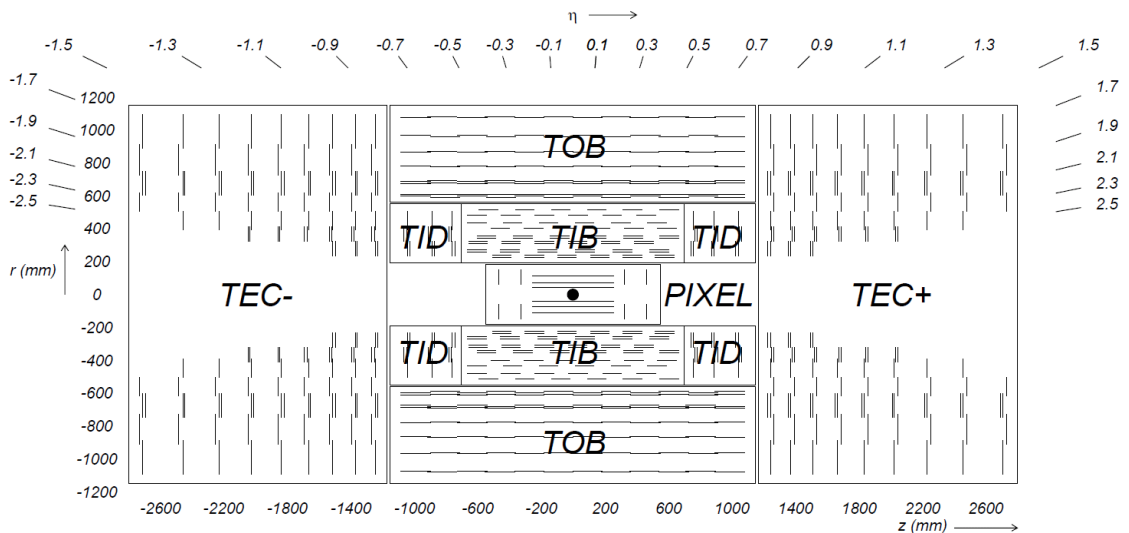


Figure 1.4: Schematic sketch of the silicon tracker at CMS in the $z - \phi$ plane including the silicon pixel detector (PIXEL) as well as the different components of the silicon strip detector: tracker inner barrel (TIB), tracker outer barrel (TOB), tracker endcap (TEC), and tracker inner disk (TID). Taken from [17].

⁸⁴ pixel system of 52×80 pixels, which are read out in double columns (see [18] on detailed
⁸⁵ information of the readout electronics). A visualisation of a part of a pixel module is
⁸⁶ shown in Fig. 1.5. In total, there are 65 million pixels comprised in the pixel detector.
⁸⁷ The large number of pixels and their small size ensure a low occupancy close to the vertex
⁸⁸ of around 0.002 – 0.02% [17] and a high hit efficiency of around 99% [19].

⁸⁹ The silicon pixel detector is very important for the reconstruction of primary and sec-
⁹⁰ ondary vertices as well as the reconstruction of particle tracks. Therefore, a high spatial
⁹¹ resolution is needed. This is achieved by the small size of the pixels ($150 \times 100 \mu\text{m}^2$) and
⁹² the exploitation of the spread of the energy deposition across several pixels (in average
⁹³ the energy is deposited across 3–5 pixels [20]). Exploiting the energy spread across pixels,
⁹⁴ a spatial resolution in the barrel region of $9.4 \mu\text{m}$ in the $r - \phi$ plane and - dependent on
⁹⁵ the incident angle of a track - a hit resolution between $20 - 45 \mu\text{m}$ in the z-direction is
⁹⁶ achieved [17]. The spatial resolution of the primary vertex depends on the number of
⁹⁷ tracks taken into account for the reconstruction of the primary vertex. For more than 50
⁹⁸ tracks originating from the primary vertex the spatial resolution is around $10 - 12 \mu\text{m}$ for
⁹⁹ each of the three spatial dimensions [17]. The reconstruction efficiency of primary vertices
¹⁰⁰ is close to 100% if more than two tracks are used for the vertex reconstruction [17].

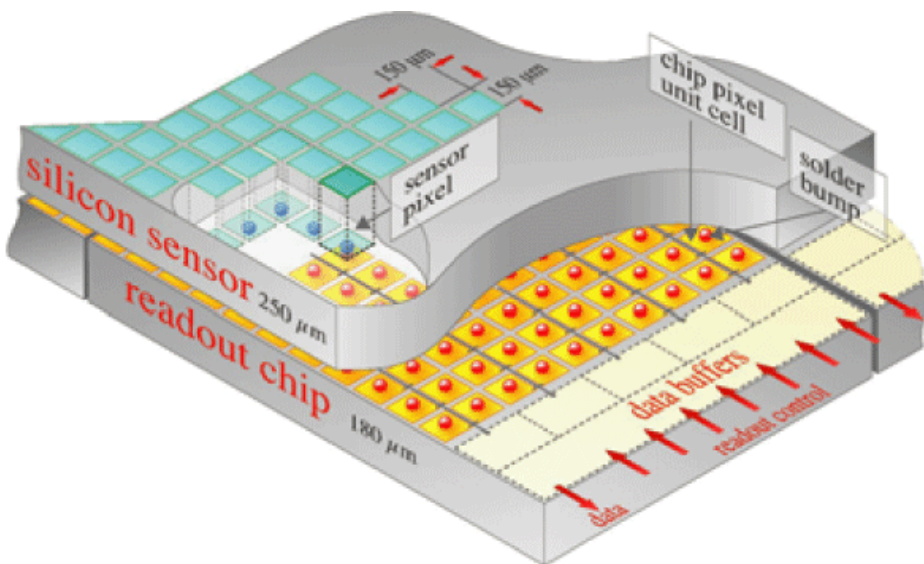


Figure 1.5: Schematic sketch of a part of a silicon pixel tracker module including the silicon sensors and the read-out-chip (ROC). Taken from [17].

101 The silicon strip tracker

102 The silicon strip tracker is the next-to innermost detector of the CMS detector and ranges
 103 up to a radius of 1.1 m. The barrel region consists of a tracker inner barrel (TIB) and a
 104 tracker outer barrel (TOB). The TIB has four layers with two layers equipped with stereo
 105 modules to measure the hit position additionally in the $r - z$ plane. The silicon sensors
 106 in the TIB are of $320\ \mu\text{m}$ thickness with a strip pitch varying between $80 - 120\ \mu\text{m}$. The
 107 TOB has six different layers (two layers of stereo modules) with silicon sensors of $500\ \mu\text{m}$
 108 thickness and strip pitches between 120 and $180\ \mu\text{m}$.

109 The endcaps are subdivided into a tracker endcap (TEC) and a tracker inner disk (TID).
 110 They ensure a coverage of a pseudorapidity up to $|\eta| = 2.5$. In each TEC, 9 disks between
 111 a z-position of $120\ \text{cm} < z < 280\ \text{cm}$ are contained. Each of the TID comprises three disks
 112 between $60\ \text{cm} < z < 110\ \text{cm}$.

113 In the barrel region, a single-point resolution between $23 - 52\ \mu\text{m}$ in the $r - \phi$ plane and
 114 $230 - 530\ \mu\text{m}$ in the z-direction is achieved.

115 Energy measurements in the tracking system

116 A charged particle traversing the above mentioned silicon detectors produces electron-
 117 hole pairs in the semiconducting material along its trajectory, thus loosing energy due to
 118 ionisation. For silicon, the mean energy to create an electron-hole pair is 3.61 eV at -10°C .
 119 Minimally ionising particles produce an average of 22 000 electron-hole pairs in silicon
 120 sensors [18]. Electrons that are subject to a hard collision with the incoming particle
 121 (so-called delta-rays), produce further ionisation and can thus lead to much higher energy
 122 deposits in the silicon. Because of the applied bias voltage at the sensors (for the creation
 123 of a depletion zone), the released electrons (holes) travel to the n-contacts (p-contacts),
 124 thereby inducing a current which is measured by the readout electronics. A more detailed
 125 description of the energy measurement in silicon sensors can be found in [18].

126 1.2.2 The electromagnetic calorimeter

127 The electromagnetic calorimeter (ECAL) [14, 21] encloses the tracking system and starts
 128 at a radius of 129 cm in the barrel region. It is divided into a barrel part and two endcaps,
 129 which are at a distance of 314 cm from the vertex. Figure 1.6 depicts a schematic sketch
 130 of the electromagnetic calorimeter system in the transverse plane. It can be seen, that
 131 the ECAL barrel (EB) covers a pseudorapidity region up to $|\eta| = 1.479$. The ECAL
 132 endcaps (EE) start at $|\eta| = 1.653$ and reach up to $|\eta| = 3.0$. Before the endcaps, a
 133 preshower detector ($1.653 < |\eta| < 2.6$) is installed with the main task to identify neutral
 134 pions in the endcaps. It additionally improves the position measurement of electrons and
 135 photons.

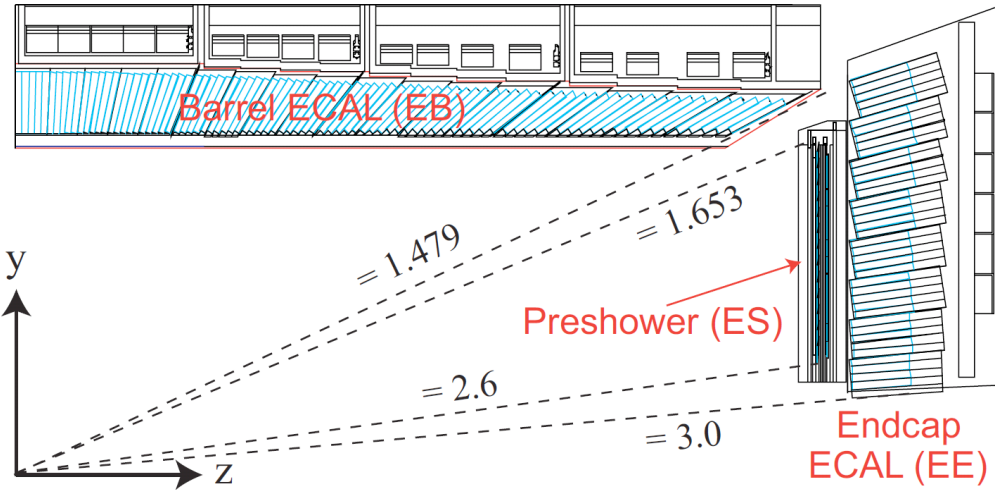


Figure 1.6: A quarter section of the ECAL in a transverse view. Taken from [14].

The EB and EE consist of lead tungstate (PbWO_4) scintillating crystals, 61200 in the barrel region and 7324 in the endcaps. Their advantage is the short radiation length ($X_0=0.89\text{ cm}$) and a small Molière radius (2.2 cm). Thus, particles deposit their energy on rather short distances and a compact design is possible. To detect the rather low light yield ($30\gamma/\text{MeV}$) of a traversing particle, silicon avalanche photodiodes (APDs) are used in the barrel region and vacuum phototriodes (VPTs) in the endcaps. For information on the readout electronics, the reader is referred to [14].

The resolution of an energy measurement in the calorimeter can be expressed by

$$\left(\frac{\sigma}{E}\right)^2 = \left(\frac{S}{\sqrt{E}}\right)^2 + \left(\frac{N}{E}\right)^2 + C^2, \quad (1.3)$$

with S referring to the stochastic term, N to the noise term, and C to a constant term. For the ECAL the parameters of Eq. (1.3) are measured to $S = 3.63\sqrt{\text{GeV}}$, $N = 0.124\text{ GeV}$, and $C = 0.26$ [14]. These numbers lead to an energy resolution of around 0.4% for an electron with $E \approx 200\text{ GeV}$ and around 0.6% for an electron with $E \approx 50\text{ GeV}$.

1.2.3 The hadronic calorimeter

The hadronic calorimeter (HCAL) [14,22] of the CMS detector is splitted into four different detector modules: the hadron barrel (HB), the hadron outer (HO), the hadron endcap (HE) and the hadron forward (HF) calorimeters. A schematic sketch is depicted in Fig. 1.7.

The HCAL is dedicated to measuring the energy of hadrons as well as providing a good estimate of the missing energy in the event. The latter one is achieved by the

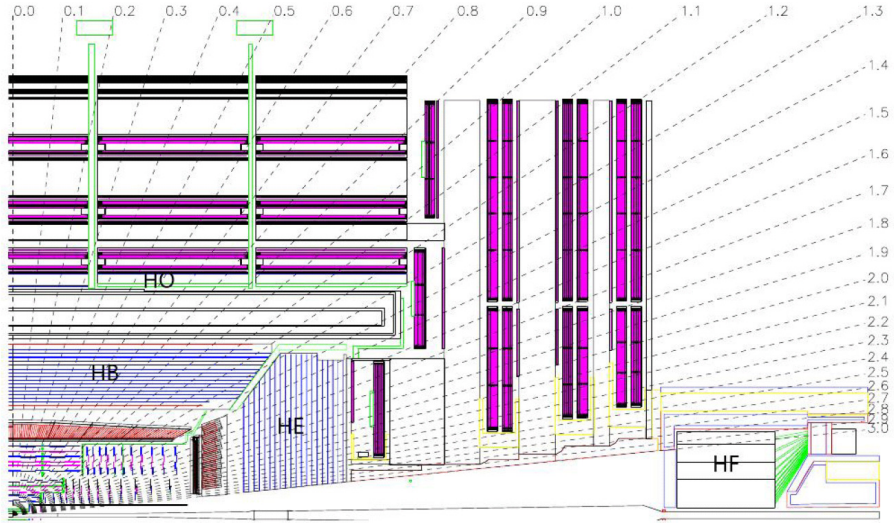


Figure 1.7: A quarter section of the HCAL in a transverse view. Taken from [23].

155 high pseudorapidity coverage ($|\eta| < 5.0$) that assures the detection of most of the visible
156 particles.

157 The HCAL is a so-called sampling calorimeter which consists of brass absorber material,
158 initiating the hadronic shower, as well as active plastic scintillators. The emitted photons
159 are read out with wavelength-shifting (WLS) fibres which are embedded into the scintil-
160 lators. These in turn are connected to clear fibres that transfer the light to the readout
161 system.

162 The hadron barrel (HB) covers the pseudorapidity range between $-1.4 < \eta < 1.4$. It
163 is composed of 17 layers of absorber material (15 brass and 2 steel layers) interleaved
164 with scintillator layers. The scintillator layers are divided into 2304 towers with a size of
165 $\Delta\eta \times \Delta\phi = 0.087 \times 0.087$.

166 The hadron outer (HO) covers a pseudorapidity range up to $|\eta| = 1.26$ and is divided
167 into sectors which match the ϕ segmentation of the drift-tube chambers of the muon
168 system (see Section 1.2.4). It is located between the solenoid and the barrel detector of
169 the muon system. The HO is dedicated to measuring the energy of the shower leakage of
170 hadrons. Its thickness corresponds to over ten interaction lengths.

171 The hadron endcap (HE) extends the pseudorapidity coverage of the HCAL up to $|\eta| =$
172 3.0 and starts at $|\eta| = 1.3$. It consists of 2304 towers in total, which vary in size between
173 $5 - 10^\circ$ in the ϕ direction and $0.087 - 0.35$ in η direction.

174 Finally, the hadron forward (HF) calorimeter extends the pseudorapidity range up to
175 $|\eta| = 5.0$, starting from $|\eta| = 3.0$. It is build out of steel plates, which contain 1 mm^2
176 grooves containing quartz fibres. The emitted light by the quartz fibres is transferred to
177 photomultipliers. The HF is divided into 13 towers where almost all towers have a spread

¹⁷⁸ of $\Delta\eta \approx 0.175$ in η direction and $\sim 10^\circ$ in ϕ direction.

¹⁷⁹ 1.2.4 The muon system

¹⁸⁰ The muon system [14,24] is the outermost detector component at CMS. It comprises three
¹⁸¹ different types of gaseous detectors, mounted into the iron return yokes: drift tube (DT)
¹⁸² chambers in the barrel region ($|\eta| < 1.2$), cathode strip chambers (CSC) in the endcap
¹⁸³ region ($1.04 < |\eta| < 2.4$) and resistive plate chambers (RPC) in the barrel as well as the
¹⁸⁴ endcap region ($|\eta| < 1.6$) (see Fig. 1.8 for a schematic sketch of the muon system). In
¹⁸⁵ the barrel part of the muon system, four layers (so-called stations) of drift-tube chambers
¹⁸⁶ are assembled inside the iron return yoke layers at radii of 4.0, 4.9, 5.9 and 7.0 m from
¹⁸⁷ the beam axis. The position of a muon traversing these layers can be measured with a
¹⁸⁸ precision of $\approx 100 \mu\text{m}$ in radial direction and $\approx 1 \text{ mrad}$ in ϕ direction.

¹⁸⁹ The four endcap disks are made up of 468 cathode strip chambers in total. By measuring
¹⁹⁰ the centre-of-gravity, they achieve a spatial resolution of $\approx 100 - 200 \mu\text{m}$ and an angular
¹⁹¹ resolution of $\approx 10 \text{ mrad}$ in ϕ direction. They are designed in order to cope with a high
¹⁹² particle flux of about $1\text{kHz}/\text{cm}^2$ and a non-uniform magnetic field. As signals can be
¹⁹³ transferred very fast, they are used for the level-1 trigger system.

¹⁹⁴ Finally, the resistive plate chambers cover the barrel as well as the endcap region up to
¹⁹⁵ a pseudorapidity of $\eta = 1.6$. They provide a fast response with a good time resolution
¹⁹⁶ enabling the exact identification of the respective bunch-crossing. It is used for the level-1

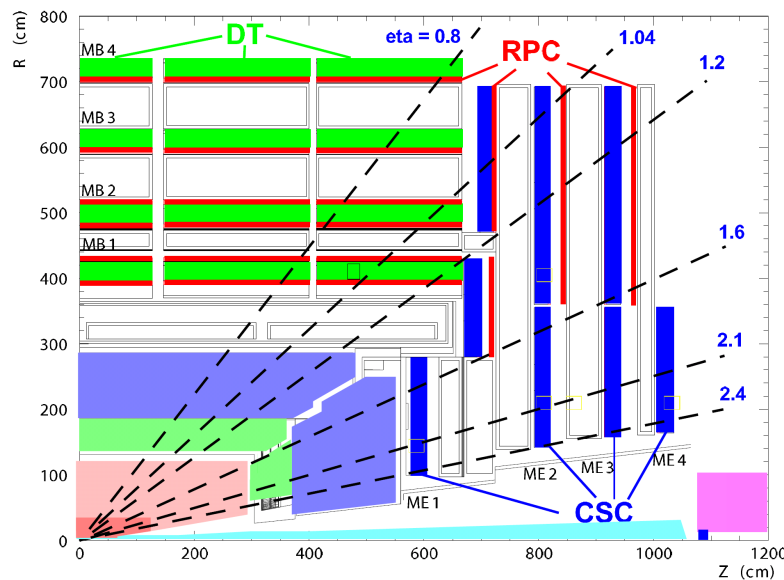


Figure 1.8: A quarter section of the CMS detector in the transverse plane with a detailed view on the muon system. Taken from [14].

197 trigger system as well.

198 1.2.5 The trigger system

199 Because of the impossibility of storing each event occurring at the CMS experiment, a
200 multistage trigger system [14] is used to achieve a drastic reduction of recorded events
201 by nearly six orders of magnitude. It comprises two main parts: a so-called level-1 (L1)
202 trigger system and a high-level trigger (HLT) system.

203 The L1 triggers need to provide a very fast decision ($3.2\ \mu\text{s}$, where around $1\ \mu\text{s}$ is al-
204 located to the actual L1 trigger calculations) whether an event shall be recorded or not.
205 During this time, the recorded event data is held in buffers located close to the single
206 detector components. Information from the muon system and the calorimeters is used for
207 the L1-trigger decisions. Objects used for these decisions are so-called “trigger primitive”
208 objects: photons, electrons, muons, jets above certain E_T and p_T thresholds and global
209 variables like missing transverse energy, \cancel{E}_T . The design value of the number of events per
210 second that pass this trigger stage is 100 kHz.

211 After a time of $3.2\ \mu\text{s}$, the stored data in the buffers close to the single detector com-
212 ponents are transferred to the front-end readout buffers in case the event passed the
213 L1-trigger requirements. By partial event reconstruction and the use of various trigger
214 levels (calorimeter, muon information followed by pixel information and full event recon-
215 struction), higher event objects can be used to check whether HLT-trigger requirements
216 are fulfilled. On HLT level, the decision time amounts to 50 ms and a reduction from
217 100 kHz to 100 Hz of event recording is achieved.

218 1.3 Event reconstruction and particle identification

219 A crucial ingredient of data analysis at the CMS experiment, is the translation of the
220 energy measurements in the various sub-detector components into physical objects, like
221 muons, electrons, etc. . For this translation, i. e. particle identification, information from
222 all detector components are used. This is known as the particle-flow event reconstruction
223 algorithm [25]. In Fig. 1.9, a slice through the CMS detector is shown with the signatures
224 of different particles indicated as coloured lines.

225 In the next section an introduction into this algorithm is given, followed by the definition
226 and classification of physics objects at the CMS experiment.

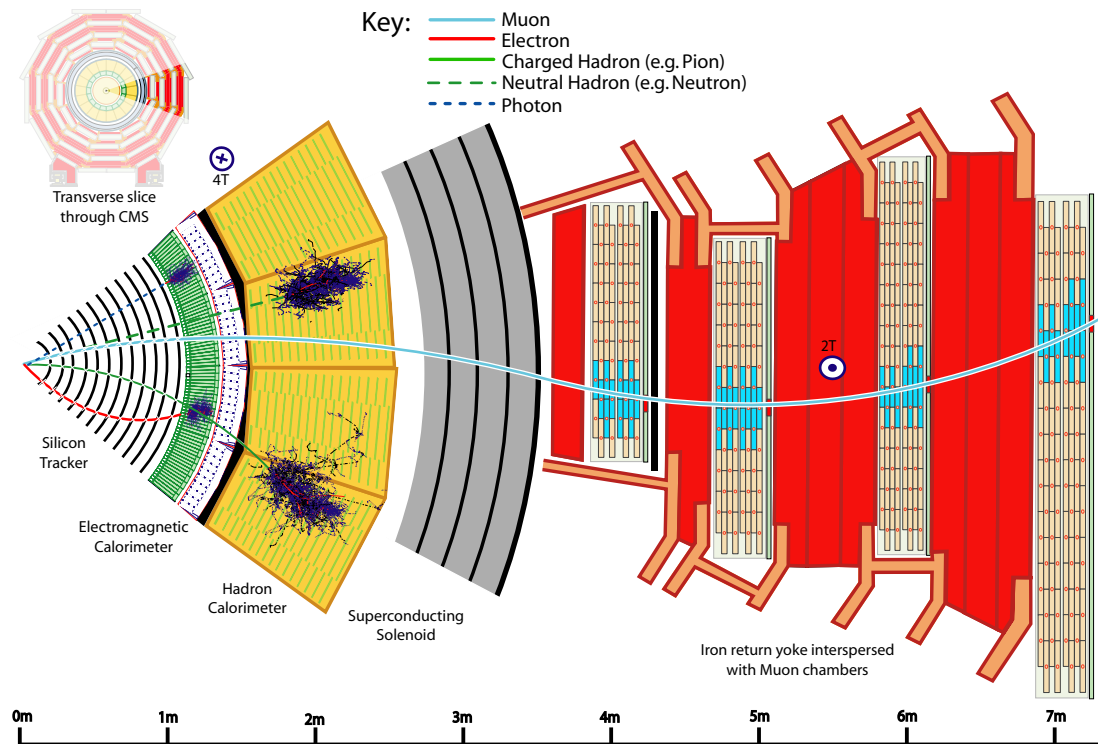


Figure 1.9: A radial slice through the CMS detector with several particle signatures indicated as coloured lines.

²²⁷ 1.3.1 The particle-flow algorithm

²²⁸ The particle-flow (PF) event description [25] aims at optimising particle identification
²²⁹ by the usage of all sub-detector components of the CMS detector. There are three main
²³⁰ building bricks used for the global event description: reconstructed charged-particle tracks,
²³¹ calorimeter clusters, and muon tracks. The main requirements for these building bricks is
²³² a high reconstruction efficiency as well as a small fake rate. Therefore, a special emphasis
²³³ was put on developing a very efficient tracking algorithm (see Section 1.3.2) and a well
²³⁴ performing calorimeter clustering algorithm [25].

²³⁵ The particle-flow algorithm proceeds as follows in an event (the following steps are a
²³⁶ bit simplistic, the reader is referred to [25] for a detailed discussion):

- ²³⁷ 1. For each pair of detected building bricks, a distance in the $\eta - \phi$ plane is calculated
²³⁸ in order to quantify the quality of their link (whether the two building bricks stem
²³⁹ from the same particle).
- ²⁴⁰ 2. “Blocks” are produced from the building bricks that are linked together (with a
²⁴¹ typical number of one, two or three building bricks contained in a block).

- 242 3. For each block the following steps are performed:
- 243 a) Each global muon (hits detected in the tracker as well as in the muon system)
 244 where the p_T measured in both sub-detectors is compatible with the tracker
 245 measurement only is defined as particle-flow muon and the track in both sub-
 246 detectors is removed from the event.
- 247 b) Electron reconstruction and identification follows using blocks with tracker hits
 248 and ECAL clusters. For an identified particle-flow electron, the corresponding
 249 tracker hits and the ECAL clusters (including energy deposits from Brems-
 250 strahlung photons) are removed.
- 251 c) Tighter tracker quality criteria are applied.
- 252 d) The compatibility of the remaining ECAL and HCAL energy deposits to trans-
 253 verse momentum of the reconstructed tracks within a block is checked. This
 254 allows for the identification of particle-flow charged hadrons with a momentum
 255 estimate using tracker and calorimeter information. Only, if the energy deposits
 256 in the ECAL or HCAL are much larger than the corresponding track p_T , it gives
 257 rise to a particle-flow photon or particle-flow neutral hadron. All used ECAL
 258 and HCAL clusters used for the identification as well as the reconstructed tracks
 259 are removed from the event.
- 260 e) Finally, the remaining HCAL and ECAL clusters (which are all not linked
 261 to any other building block) give rise to particle-flow photons or particle-flow
 262 neutral hadrons.
- 263 These identified particle-flow objects are used to identify further objects in the event, e.g.
 264 the missing transverse-energy or decay products of a tau lepton.

265 **1.3.2 Object reconstruction**

266 In this section, an overview about the required criteria for the identification of particles
 267 and other physics object is given.

268 **Reconstruction of tracks**

269 The reconstruction of tracks aims at linking several hits in the tracking system to one
 270 reconstructed track that matches with a high probability the original trajectory of the
 271 particle. With the track reconstruction an estimate of the particle's momentum as well as
 272 the position can be achieved. The challenge arise due to the high combinatorial complexity
 273 because of the large number of hits detected in each event, especially in the layers close to
 274 the interaction vertex. In the following an overview about the tracking algorithm used at

275 CMS is given. The reader is referred to [17] for a thorough description of the reconstruction
 276 of tracks at CMS.

277 The developed tracking software used at CMS is usually referred to as the Combinatorial
 278 Track Finder (CTF). It grounds on the so-called combinatorial Kalman filter [26–28], which
 279 is mathematically equivalent to a global least square minimisation for linear models with
 280 Gaussian noise.

281 The basic idea of the tracking algorithm at CMS is to not apply the combinatorial
 282 Kalman filter on all hits in one step but to reduce the level of complexity by an iterative
 283 procedure (called iterative tracking). A reduction of complexity can be achieved by re-
 284 constructing tracks in the first step that are easy to identify because of e.g. a high p_T .
 285 These tracks are removed afterwards and the remaining tracker hits are subject to further
 286 reconstruction iterations. The following iterations are performed:

- 287 • Iteration 0: Tracks near to the pp interaction point that have three pixel hits and a
 288 $p_T > 0.8 \text{ GeV}$ are reconstructed.
- 289 • Iteration 1: Tracks with only two pixel hits and $p_T > 0.8 \text{ GeV}$ are recovered.
- 290 • Iteration 2: Low p_T tracks from the pp interaction point are reconstructed.
- 291 • Iteration 3-5: Reconstruction of tracks that are not originating from the primary
 292 vertex and recovering of tracks not found by previous iterations

293 Within these iterations, the reconstruction is subdivided into four different steps:

- 294 • Seed generation: Only 2-3 hits are used to define track candidates.
- 295 • Extrapolation: Based on expected flight path, additional hits are assigned to the
 296 candidate track (use of Kalman filter)
- 297 • Parameter estimates: With the usage of the Kalman filter and a smoother the tra-
 298 jectory parameters are determined
- 299 • Setting of quality flags: Quality flags are assigned to all tracks and tracks that fail
 300 certain quality criteria are discarded.

301 The configuration of the first and the fourth step differ across the different iterations.

302 **Reconstruction of jets**

303 The reconstruction of jets is done by a anti-kt method at CMS.

- 304 • Clustering methods: anti kt method
- 305 • jet energy corrections

306 1.3.2.1 Reconstruction of muons

307 There are three different muon definitions at CMS [29]: global muons (correspond to
 308 particle-flow muons), tracker muons, and standalone muons. They have all in common
 309 that they require energy deposits in the muon system. The reconstruction of each of the
 310 three muon types is explained in the following.

311 **Standalone muons:** For the reconstruction of standalone muons, all reconstructed seg-
 312 ments in the muon system are utilised. Similar to the track reconstruction in the
 313 tracking system, Kalman filter techniques [30] are exploited to reconstruct muon tra-
 314 jectories in the muon chambers. A compatibility to the interaction point is imposed
 315 to reconstruct only muons produced at the LHC (no cosmic muons). Further details
 316 about the reconstruction of standalone muons can be found in [14, 31]

317 **Tracker muons:** To reconstruct so-called tracker muons, all tracker tracks with a $p_T >$
 318 0.5 GeV and $p > 2.5 \text{ GeV}$ are extrapolated to the muon system. If at least one muon
 319 segment is matched to a reconstructed track within certain quality criteria, the
 320 trajectory is considered as a tracker muon (see [29] for more detailed information).

321 **Global muons:** For the reconstruction of global muons an outside-in approach is
 322 utilised. For each reconstructed standalone muon, the compatibility to the recon-
 323 structed tracks in the tracking system is checked. If compatible, a global muon track
 324 is reconstructed using Kalman filter techniques. For high- p_T muons, the momentum
 325 resolution can be increased compared to the momentum estimated using tracker
 326 information only [29].

327 1.3.2.2 Reconstruction of electrons

328 The reconstruction of electrons at the CMS experiment is based on a mixture of the
 329 particle-flow algorithm explained in Section 1.3.1 and a standalone approach [32]. Thus,
 330 it is a very complex procedure and a complete description would go beyond the scope of this
 331 thesis. Therefore, only the rough idea of the electron reconstruction shall be reviewed here.
 332 The reader is referred to [33] for a complete description of the reconstruction procedure.

333 The difficulty of the electron reconstruction lies in the possibly large energy losses due
 334 to bremsstrahlung. This can change the direction of the electron significantly and lead to
 335 a reduced efficiency of the standard track reconstruction used for tracker tracks. There-
 336 fore, an optimised track reconstruction for electrons is performed in order to account for
 337 direction changes due to the radiation of photons. Because the dedicated electron track
 338 reconstruction can be very time consuming, a seeding of tracker hits rely already on ECAL
 339 information to reduce the number of candidate tracks.

³⁴⁰ **Reconstruction of taus**

³⁴¹ **Reconstruction of missing transverse energy**

³⁴² **Event cleaning**

³⁴³ **1.4 Event simulation**

³⁴⁴ Needed:

³⁴⁵ • Some information on simulation

³⁴⁶ • PDF !

³⁴⁷ 3-4 pages

348

Part 2

349

Summary

350 In the year 2012, a variety of different searches and measurements were performed
351 at the CMS experiment. A strong focus was set on the search for physics beyond the
352 Standard Model as well as the measurement of Standard Model parameters and important
353 performance parameters of the CMS detector. This thesis contributed in a twofold way
354 to the physics program of CMS.

355 First, a search for physics beyond the Standard Model by the selection of highly ionising,
356 short tracks was performed. The design of the search was strongly motivated by super-
357 symmetric extensions of the Standard Model that include long-lived charginos decaying
358 inside the tracker into the lightest supersymmetric particle, the neutralino. Because of
359 the higher masses of supersymmetric particles, the chargino is expected to deposit much
360 higher amounts of energies in the tracking system compared to the Standard Model back-
361 ground. Additionally, the search targeted supersymmetric models with chargino lifetimes
362 of the order of $c\tau \approx 1 - 30$ cm where most of the charginos even decay in the first layers of
363 the tracker. Therefore, for the first time, reconstructed tracks down to three tracker hits
364 were incorporated and an energy measurement was performed. For this purpose, energy
365 information from the silicon pixel detector was exploited for the first time at CMS. This
366 could only be done by an energy calibration of the pixel tracker which was performed
367 within this thesis.

368 This search could exclude supersymmetric models with long-lived charginos down to
369 lifetimes of xxx for a mass of 100 GeV and down to xxx for 500 GeV charginos. Current
370 limits could be confirmed and slight improvements of the order of 10-30 GeV were achieved.
371 The major challenge of this search consisted in the estimation of the Standard Model
372 background because of the low event yield in most of the control regions. Therefore, the
373 search sensitivity is mainly limited by systematic uncertainties arising from limited size of
374 simulated samples as well as control regions in data.

375 The second contribution of this thesis contains the measurement of the jet transverse-
376 momentum resolution at 8 TeV at the CMS detector. The jet p_T resolution is a crucial
377 ingredient for analyses at CMS relying on a good understanding of the quality of the jet p_T
378 measurement, e.g. physics beyond the Standard Model where QCD-multijet background
379 plays a major role or Standard Model measurements of the QCD cross section or top
380 quark differential measurements. The method of the resolution measurement based on
381 earlier methods but is the first measurement that accounted for the fundamental non-
382 Gaussian behaviour of the measured resolution in exclusive bins of further jet activity.
383 The gaussian behaviour can be recovered when dividing the events by the direction of
384 further jets in the event.

385 Impressive achievements could be achieved.

- 386 • Why are the main achievements in both of the analyses
387 • What are the main results in both of the analyses

- 388 • Paper in preparation for the resolution measurement
- 389 • Schoener Abschlussatz

390 Bibliography

- [1] L. Evans and P. Bryant, “LHC Machine”, *JINST* **3** (2008) S08001.
doi:10.1088/1748-0221/3/08/S08001.
- [2] O. S. Bruning, P. Collier, P. Lebrun et al., “LHC Design Report Vol.1: The LHC Main Ring”, *Technical Design Report CERN-2004-003* (2004).
- [3] “LEP Design Report: Vol.2. The LEP Main Ring”,.
- [4] CERN, “CERN, public web page”. www.cern.ch. Accessed: 2016-01-17.
- [5] CERN, “LHC: the guide”, *CERN Brochure CERN-Brochure-2009-003-Eng* (2009).
- [6] CMS Collaboration, “The CMS experiment at the CERN LHC”, *JINST* **3** (2008) S08004. doi:10.1088/1748-0221/3/08/S08004.
- [7] CMS Collaboration, “CMS physics: Technical design report”, *Technical Design Report CERN-LHCC-2006-001, CMS-TDR-008-1* (2006).
- [8] ATLAS Collaboration, “The ATLAS Experiment at the CERN Large Hadron Collider”, *JINST* **3** (2008) S08003. doi:10.1088/1748-0221/3/08/S08003.
- [9] ATLAS Collaboration, “ATLAS: Detector and physics performance technical design report. Volume 1”, *Technical Design Report CERN-LHCC-99-14,ATLAS-TDR-14* (1999).
- [10] ATLAS Collaboration, “ATLAS: Detector and physics performance technical design report. Volume 2”, *Technical Design Report CERN-LHCC-99-15, ATLAS-TDR-15* (1999).
- [11] LHCb Collaboration, “The LHCb Detector at the LHC”, *JINST* **3** (2008) S08005. doi:10.1088/1748-0221/3/08/S08005.
- [12] ALICE Collaboration, “The ALICE experiment at the CERN LHC”, *JINST* **3** (2008) S08002. doi:10.1088/1748-0221/3/08/S08002.
- [13] CMS Collaboration, “CMS Luminosity - Public Results”, *Public CMS Wiki* (2015). <https://twiki.cern.ch/twiki/bin/view/CMSPublic/LumiPublicResults>, Topic revision: r111.

- ⁴¹⁸ [14] CMS Collaboration, “CMS Physics: Technical Design Report Volume 1: Detector
⁴¹⁹ Performance and Software”, *Technical Design Report*
⁴²⁰ **CERN-LHCC-2006-001,CMS-TDR-8-1** (2006).
- ⁴²¹ [15] CMS Collaboration, “The CMS tracker system project: Technical Design Report”,
⁴²² *Technical Design Report* **CERN-LHCC-98-006,CMS-TDR-5** (1997).
- ⁴²³ [16] CMS Collaboration, “The CMS tracker : addendum to the Technical Design
⁴²⁴ Report”, *Technical Design Report* **CERN-LHCC-2000-016** (2000).
- ⁴²⁵ [17] CMS Collaboration, “Description and performance of track and primary-vertex
⁴²⁶ reconstruction with the CMS tracker”, *JINST* **9** (2014), no. 10, P10009,
⁴²⁷ arXiv:1405.6569. doi:10.1088/1748-0221/9/10/P10009.
- ⁴²⁸ [18] J. A. Sibille, “Radiation Hard Hybrid Pixel Detectors, and a bbbar Cross Section
⁴²⁹ Measurement at the CMS Experiment”. PhD thesis, Hamburg University, 2013.
⁴³⁰ <http://cds.cern.ch/record/1569832>.
- ⁴³¹ [19] CMS Collaboration, “Offline calibrations and performance of the CMS pixel
⁴³² detector”, *Nucl. Instrum. Meth.* **A650** (2011) 25–29.
⁴³³ doi:10.1016/j.nima.2010.11.188.
- ⁴³⁴ [20] CMS Collaboration, “Pixel Performance plots for 2012 data and simulation”, *Public
⁴³⁵ CMS Wiki*. <https://twiki.cern.ch/twiki/bin/view/CMSPublic/PixelOfflinePlots2013>,
⁴³⁶ Topic revision: r22.
- ⁴³⁷ [21] CMS Collaboration, “The CMS electromagnetic calorimeter project: Technical
⁴³⁸ Design Report”, *Technical Design Report* **CERN-LHCC-97-033,CMS-TDR-4**
⁴³⁹ (1997).
- ⁴⁴⁰ [22] CMS Collaboration, “The CMS hadron calorimeter project: Technical Design
⁴⁴¹ Report”, *Technical Design Report* **CERN-LHCC-97-031,CMS-TDR-2** (1997).
- ⁴⁴² [23] CMS Collaboration, “Performance of CMS Hadron Calorimeter Timing and
⁴⁴³ Synchronization using Test Beam, Cosmic Ray, and LHC Beam Data”, *JINST* **5**
⁴⁴⁴ (2010) T03013, arXiv:0911.4877. doi:10.1088/1748-0221/5/03/T03013.
- ⁴⁴⁵ [24] CMS Collaboration, “The CMS muon project: Technical Design Report”, *Technical
⁴⁴⁶ Design Report* **CERN-LHCC-97-032,CMS-TDR-3** (1997).
- ⁴⁴⁷ [25] CMS Collaboration, “Particle-Flow Event Reconstruction in CMS and Performance
⁴⁴⁸ for Jets, Taus, and MET”, *CMS Physics Analysis Summary*
⁴⁴⁹ **CMS-PAS-PFT-09-001** (2009).

- 450 [26] P. Billoir, “Progressive track recognition with a Kalman like fitting procedure”,
451 *Comput. Phys. Commun.* **57** (1989) 390–394.
452 doi:10.1016/0010-4655(89)90249-X.
- 453 [27] P. Billoir and S. Qian, “Simultaneous pattern recognition and track fitting by the
454 Kalman filtering method”, *Nucl. Instrum. Meth.* **A294** (1990) 219–228.
455 doi:10.1016/0168-9002(90)91835-Y.
- 456 [28] R. Mankel, “A Concurrent track evolution algorithm for pattern recognition in the
457 HERA-B main tracking system”, *Nucl. Instrum. Meth.* **A395** (1997) 169–184.
458 doi:10.1016/S0168-9002(97)00705-5.
- 459 [29] CMS Collaboration, “Performance of CMS muon reconstruction in pp collision
460 events at $\sqrt{s} = 7$ TeV”, *JINST* **7** (2012) P10002, arXiv:1206.4071.
461 doi:10.1088/1748-0221/7/10/P10002.
- 462 [30] R. Frhwirth, “Application of Kalman filtering to track and vertex fitting”, *Nucl.*
463 *Instrum. Meth.* **A262** (1987) 444–450. doi:10.1016/0168-9002(87)90887-4.
- 464 [31] CMS Collaboration, “Performance of CMS Muon Reconstruction in Cosmic-Ray
465 Events”, *JINST* **5** (2010) T03022, arXiv:0911.4994.
466 doi:10.1088/1748-0221/5/03/T03022.
- 467 [32] S. Baffioni, C. Charlot, F. Ferri et al., “Electron reconstruction in CMS”, *Eur.*
468 *Phys. J.* **C49** (2007) 1099–1116. doi:10.1140/epjc/s10052-006-0175-5.
- 469 [33] CMS Collaboration, “Performance of electron reconstruction and selection with the
470 CMS detector in proton-proton collisions at $\sqrt{s} = 8$ TeV”, *JINST* **10** (2015), no. 06,
471 P06005, arXiv:1502.02701. doi:10.1088/1748-0221/10/06/P06005.